Computationally efficient coarse-graining XDEM/CFD modeling of fixed-bed combustion of biomass

Combustion and Flame 238 (2022) 111876

Contents lists available at ScienceDirect

Combustion and Flame

journal homepage: www.elsevier.com/locate/combustflame

Computationally efficient coarse-graining XDEM/CFD modeling of fixed-bed combustion of biomass

Jingyuan Zhang [a], Tian Li [a,b,*], Henrik Ström [c,a], Terese Løvås [a]

[a] Department of Energy and Process Engineering, Faculty of Engineering, NTNU — Norwegian University of Science and Technology, Trondheim, Norway
[b] RISE Fire Research, Tiller 7092, Norway
[c] Division of Fluid Dynamics, Department of Mechanics and Maritime Sciences, Chalmers University of Technology, SE-412 96 Gothenburg, Sweden

ARTICLE INFO

Article history:
Received 16 November 2020
Revised 10 November 2021
Accepted 11 November 2021

Keywords:
CFD
Biomass
Fixed-bed combustion
Coupling

ABSTRACT

In the multi-scale modeling of a dense particle system, the particle phase and the gas phase can be modeled on vastly different scales. The coupling between the two models has a critical influence on the predictions obtained from the combined framework but can be accomplished in a variety of ways under different assumptions. In this work, a transient 3D model using a new coupling approach for fixed-bed combustion of biomass is presented. The developed model is formulated as an Eulerian-Lagrangian framework. A particle grid, generated based on the fluid grid, is applied as a transfer grid, and a diffusion operation is implemented to smooth the interactions between the gas phase and the particles. The interactions between gas and solid phases as well as the radiative heat transfer between particles are considered. The particle motion is resolved by the soft-sphere model, whereas the conversion is calculated based on a thermally thick particle model. All sub-models are optimized to enhance computational efficiency. The 3D model is validated by comparing the simulations with laboratory-scale experiments for a fixed-bed operated in counter-current combustion mode. The key simulation parameters are configured by sensitivity analysis. The simulation results are in good agreement with the experimental measurements, and the combustion regimes with different air inlet conditions are well captured. The coupling effects are discussed in detail. The particle grid size influences the prediction of the transient results, and the interplay between the heat transfer mechanisms inside the fixed-bed and the coupling scheme is thoroughly analyzed. Both inter-particle radiation and gas-to-particle convection play essential roles in the heat transfer inside the fuel bed, while the inter-particle heat conduction can be neglected.

1. Introduction

As a carbon-based renewable energy resource, biomass is a substitute for fossil fuels such as coal. Power generated from biomass is mainly from thermal conversion processes. Most plants use grate-fired systems for their simplicity and versatility. The grate furnace has a low construction cost and can be operated with various feed materials with a wide range of moisture contents [1]. However, the emissions are not only due to the feed but highly influenced by the operating parameters [2]. In this respect, a better design of the grate furnace can improve combustion efficiency and reduce the emissions. The detailed information from inside the furnace that is required for optimization can be hard to measure. Complementary to experimental methods, computational fluid dynamics (CFD) simulation is an alternative tool to optimize the combustion process of a grate-fired furnace owing to its cost effectiveness and fast turnover time.

To capture the thermochemical conversion of biomass in the fuel bed and the subsequent gas phase conversion in the freeboard region, a transient multi-phase simulation is needed. There are two main approaches in conventional CFD regarding multiphase models. The first one is the Eulerian-Eulerian approach. One example using this principle is the so-called porous media model (PMM). The NavierStokes equations (including the conservation of mass, species and energy) for the gas phase are solved using a phase fraction approach, and related source terms that describe the momentum, mass and energy transfer between the gas and solid phases. The particle sub-models are registered to the computational grids to calculate the source terms. One cell can contain several identical particles or even a certain fraction of one particle [3]. The inter-particle momentum and mass transfers are usually ignored. The inter-particle heat transfer can be resolved by the par-

* Corresponding author.
E-mail address: tian.li@ntnu.no (T. Li).

https://doi.org/10.1016/j.combustflame.2021.111876

ticle sub-models on the surface heat balance, or by resolving the energy continuity equation for the solid phase, which regards the particles as a continuum [4]. PMM can be computationally efficient to deal with a large number of particles, but it requires additional sub-models to get solid properties in terms of a continuous phase from individual particles. This model approach also cannot describe the movement of particles from first principles, as the information about individual particles has been averaged out. In some studies, extra models are employed to predict bed deformation due to particle shrinkage [5].

The other approach is the Eulerian-Lagrangian approach. The gas phase is still resolved by the NavierStokes equations, while the particles are described by the extended discrete element method (XDEM). In the classical discrete element method (DEM) method, the position and motion in time and space of each particle or parcel are tracked. XDEM extends the DEM by adding properties and various processes attached to the particle. For example, the single particle thermal conversion model with the consideration of intra-particle heat transfer can be coupled to the DEM using the soft-sphere model to calculate the particle collisions. Plenty of studies of such XDEM/CFD simulations (or DEM/CFD in some literature) have been conducted in the past decade. Peters and Bruch et al. [6,7] implemented a thermally thick particle model into the DEM framework. The inter-particle heat transfer through conduction and radiation is modeled, and the simulations of biomass combustion were conducted under fixed-bed conditions. Wiese et al. [8] modeled particle collisions with cylindrically shaped particles in the DEM/CFD framework for pellets. In their simulations, a transfer grid was employed to the data transfer between gas and particles. Mahmoudi et al. [9] modeled the beech wood chips combustion in a fixed-bed in the DEM/CFD method. A good agreement between measured and simulated bed mass loss and bed temperature was obtained. Furthermore, a simulation of a plant-scale municipal solid waste (MSW) incineration on grates has been presented by Wissing et al [10].

The XDEM/CFD approach can however capture multi-physics phenomena and provide more detailed information. It is usually quite computationally costly as the particle search in the collision model and the thermally thick particle conversion model require massive calculation time when the particle number becomes large. Mehrabian et al. [11] implemented a numerically efficient particle conversion model and a particle position rearrangement strategy to reduce computational cost in a grate furnace simulation. However, the motion of the particles derived by the actual mechanical motion along with the grate and shrinkage-induced collapse is important to predict the fuel bed local ignition and flame stability.

Apart from the concern about the computational efficiency, another issue about the XDEM/CFD approach is the coupling between the two models. When the particle size is larger than the flow scale that needs to be resolved for the gas phase, the particles will be larger than one computational cell and the data transfer between the CFD model and XDEM is no longer straightforward. In conventional DEM/CFD modeling, the particle data is directly transferred between the cell in which the particle's centroid is located, because, for the gas phase the particle is still viewed as a Lagrangian point particle (LPP). Therefore, the inter-phase transfers are modeled by 0-dimensional models, and for particle conversion sub-models the assumption is that the cell should be able to provide the gas fields that are infinitely far from the particle surface. Therefore, for the coupling between the gas and large particles, special schemes for the data transfer between the particle sub-models and the sub-particle scale computational grids are required.

In fact, the coupling of æ̈large particlesg with a continuous phase is a common issue in various research fields. Sun et al. [12] made a review over the so-called æ̈coarse-grainingg methods and summarized four main methods: particle centroid method (PCM), the divided particle volume method (DPVM), the statistical kernel method (SKM) and the two-grid method (TGM). All these methods are aiming to map the particle properties generated from a Lagrangian point to an Eulerian field to smooth the coupling between the solid phase and the gas phase. This smoothing is typically intended to increase the robustness of the solver and decrease the dependence of the obtained solution on the numerical grids and settings used. However, most of these studies focused exclusively on hydrodynamics, whereas one may expect the various coupling issues to be all the more pronounced in non-isothermal reactive flows.

It is also very important that the coupling method can reconstruct the gas phase information required by the assumptions of the particle sub-model, when it is used to describe the particle conversion process under reacting conditions. It is essential to ensure the applicability of these extended sub-models in the simulation. In our previous study [13], the effects on the simulations of the single particle thermal conversion process by using different coarse-graining methods were evaluated. The study showed that the coupling scheme is an intrinsic property of the combined modeling framework and that it is extremely difficult (if not practically impossible) to choose coupling parameters that do not influence the results in any way. The challenges in coupling will be more severe in fixed-beds, due to the close packing attained in such beds. However, this issue is not studied carefully in most of the work on the simulation of the conversion of biomass in fixed-beds using the XDEM/CFD approach.

The objective of this work is to develop a computationally efficient model based on the XDEM/CFD approach for the simulation of the combustion of biomass particles. The model will be validated against experimental measurements. Special attention will be paid to the coupling between the particles and the gas phase in the combined modeling framework. The thermal conversion process in a laboratory-scale fixed-bed will be analyzed by using the simulation results.

2. Mathematical modeling

The model used in this work is in an Eulerian-Lagrangian framework developed using OpenFOAM®. The gas phase is solved using the NavierStokes equations and the heat and species transport equations. The presence of the particle is considered by introducing the phase volume fraction and the source terms into the equations with specific coupling methods, which will be described in detail in Section 2.2. The governing equations and the calculation of thermophysical properties of the gas mixture are presented in our previous work [13]. In this work, the inlet superficial gas velocity of the fixed-bed is below 0.42 m/s, so only the laminar flow regime is considered. A turbulence model can however be easily employed in the developed modeling framework. For the particle sub-models, the correlations that fit in the corresponding turbulent flow regimes are preferred. Usually, such correlations only require general flow information rather than detailed turbulence information as input. The optimization of the computational efficiency described in Section 2.4 is limited to fixed beds. If the particles have fierce motions, for example in a fluidized bed, the current model may fail in predicting the movement of the particles.

2.1. XDEM model

2.1.1. Particle motion model

The particle momentum is governed by Newton's second law. The potential ash loss due to breakage during collapses or bed motion is not considered in the current model, as well as the ash transformations, which may change the structure of the ash and

create larger agglomerates. The conventional drag force models, such as the Ergun [14] and Wen&Yu [15] drag correlations, will very likely over-predict the drag force acting on char particles with an integral thick and porous ash layer, resulting in an underestimated minimum fluidization velocity. To get rid of the interference from the drag model, and considering that in the fixed-bed, the motion of the particles is a gravity-driven process, only the gravity force and the contact forces are considered:

$$m_i \frac{d\mathbf{U}_i^p}{dt} = \sum_{j=1}^{n} \mathbf{F}_{ij}^c + \mathbf{F}_i^g, \tag{1}$$

$$I_i \frac{d\omega_i^p}{dt} = \sum_{j=1}^{n} \mathbf{M}_{ij}, \tag{2}$$

where m_i and I_i are the mass and moment of inertia of particle i, respectively, $\mathbf{U}_i^p$ is the velocity of the particle i, ω_i^p is the angular velocity of particle i, $\mathbf{F}_{ij}^c$ and $\mathbf{M}_{ij}$ are the contact force and contact torque acting on particle i by its jth contact (either with a particle or a wall), respectively, n is the number of total contacts for particle i, $\mathbf{F}_i^g$ is the gravity force acting on paticle i. The soft-sphere collision model is implemented to calculate the contact force and torque. Further details can be found in Fernandes et al. [16]. In this study, the motion of cylindrical particles are calculated as spherical particles with a volume-equivalent diameter.

2.1.2. Particle conversion model

A layer-based thermally thick particle model is employed [3,17]. The intra-particle heat transfer in the radial direction is considered. It is assumed that the conversion sub-processes: drying, devolatilization and char burnout, occur in infinitely thin fronts, and these fronts divide the particle into four layers: wet wood layer, dry wood layer, char layer and ash layer. The conversion of each sub-process is calculated by separate sub-models. The particle sub-models are provided in the Appendix, and more detailed model descriptions are presented in our previous work [13]. Still, compared with the model in [13], there are some adjustments made in this work. Firstly, a threshold of 1% of the particle's original mass is defined on every layer to determine whether to calculate heat conduction inside the layer. If the layer mass is less than the threshold, then the heat conduction equation for this layer will not be solved and the layer temperature will be assigned as the temperature at the outer front. By doing this, solving for the heat conduction in a very thin layer is avoided, and a much larger time step in calculating the particle heat transfer could be applied without causing numerical diffusion and temperature oscillations. It also greatly enhances the overall computational efficiency of the particle sub-models. It should be noted that a proper thermal-mass threshold may further optimize the calculation, which requires future investigations. Secondly, since the char burnout sub-model does not consider the competition for oxygen with the combustible gases released from the devolatilization process that results in a radial flow (Stefan flow) in this work, therefore char burnout is treated as a sequential process that may be initiated only after the devolatilization has been accomplished. Another adjustment is that in the previous work, the porosity of the ash layer is a fixed value, while in this work, the porosity is calculated by assuming the ash intrinsic density is a constant. This is due to the insights from the parameter study about the shrinkage factor η for the char burnout process, which is the volume ratio between the converted char layer and the generated ash layer [13], that is conducted in a later section. The calculated porosity is more realistic when accounting for varying shrinkage factors. All the other adjustments of the sub-models will be presented in the following sections.

2.1.3. Surface heat and mass transfer model

In this work, because the adiabatic wall boundary condition is used, the heat conduction and radiation between the wall and particle are currently neglected. The heat balance equation at particle surface is thus formulated as:

$$q_{in,i} = q_{conv,i} + \sum_{j=1}^{n} q_{cond,ji} + q_{rad,i}, \tag{3}$$

where $q_{in,i}$ is the heat flow rate into particle i through the surface, and this part of the heat causes the particle temperature to increase, and is consumed by endothermic sub-processes, such as drying. $q_{conv,i}$ is the heat exchange rate between particle i and its local surrounding gas by convection, which can be calculated as:

$$q_{conv,i} = h_c A_{p,i}(T_g - T_{p,i}), \tag{4}$$

where $A_{p,i}$ is the particle surface area, T_g and $T_{p,i}$ are the local gas temperature and particle surface temperature, respectively, and h_c is the heat transfer coefficient. For cylindrical particles in a fixed-bed, the Nusselt number (Nu) correlation proposed by Singhal et al. [18] is used in this work.

$$Nu_p = \frac{h_c d_p}{k_g} = 1.77 + 0.29\varepsilon^{-0.81} Re_p^{0.73} Pr_f^{0.50}, \tag{5}$$

where d_p is the particle diameter, k_g is the heat conductivity of the gas phase, ε is the local bed porosity.

$q_{cond,ji}$ is the heat exchange rate between particles j and i due to conduction. In a fixed-bed, conduction is mainly due to particle-particle static contact, and the equation proposed by Batchelor et al. [19] and modified by Zhou et al. [20] is adopted. The simplified conduction $q_{cond,ji}$ can be calculated as:

$$q_{cond,ji} = \frac{4r_{c,ij}\left(T_{p,j} - T_{p,i}\right)}{\left(1/k_{p,i} + 1/k_{p,j}\right)}, \tag{6}$$

where $k_{p,i}$ and $k_{p,j}$ are the heat conductivity for particles i and j, respectively, $r_{c,ij}$ is the particle-particle contact radius, which can be obtained from the DEM simulation based on the Hertz elastic contact theory. Here the Heron's formula is employed to calculate $r_{c,ij}$:

$$r_{c,ij} = \frac{2A}{d_{ij}}, \tag{7}$$

$$A = \sqrt{s(s - r_j)(s - r_i)(s - d_{ij})}, \tag{8}$$

$$s = \frac{(r_j + r_i + d_{ij})}{2}, \tag{9}$$

where r_j and r_i are the radius of particles j and i, respectively, and d_{ij} is the distance between the centroids of particles j and i.

The last term in Eq. (3), $q_{rad,i}$ is the heat exchange rate between particle i and its surrounding environment by radiation. A common practice is to create a radiation control volume, based on particle i's position, and search for the particle's immediate neighbors to calculate an equivalent local radiation temperature $T_{eq,i}$ [8,11]. Then $q_{rad,i}$ can be calculated as:

$$q_{rad,i} = \epsilon\sigma f({T_{eq,i}}^4 - T_i^4), \tag{10}$$

where ϵ, σ and f are the emissivity, the StefanBoltzmann constant and the view factor, respectively. To avoid a large number of computationally expensive particle searches, here, the immediate neighbors are approximated by the contact particles for particle i, which are already calculated in the DEM step. Assuming all the contacts can be treated equal to particle i, the equivalent local radiation temperature for particle i can be calculated as:

$${T_{eq,i}}^4 = \alpha T_g^4 + (1 - \alpha)\frac{1}{n}\sum_{j=1}^{n} T_j^4, \tag{11}$$

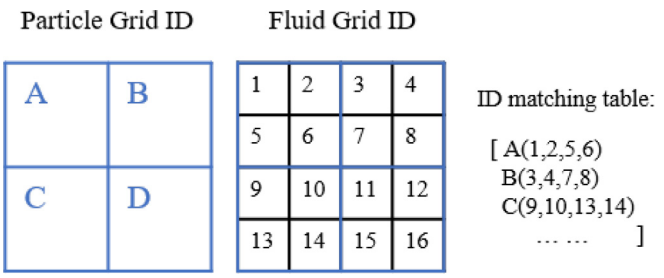

Fig. 1. Two-grid method.

where α is the gas phase fraction, and the quartic root mean is used.

The mass transfer of reactants to the particle surface is calculated through the mass transfer coefficient h_m, which is obtained by the Sherwood number (Sh). The analog of the Nu correlation is employed:

$$Sh_p = \frac{h_m d_p}{D_{e,g}} = 1.77 + 0.29\varepsilon^{-0.81} Re_p^{0.73} Sc_f^{0.50}, \tag{12}$$

where $D_{e,g}$ is the effective diffusivity of the gas phase.

2.2. Coupling between gas and particle

The coupling between the XDEM and the CFD model includes two parts. The first is to sample the gas phase properties required by the particle sub-models. Because the particles are treated as point particles in the fluid model, the details of the flow around the particles are not fully resolved. As a result, point-particle correlations are required to calculate the mass, momentum and heat exchange between the particle and the surrounding fluid. The theoretical requirements on the sampling are governed by the derivation of the sub-model itself. For example, when calculating the heat transfer using the Nu number correlation, one would want the sampling to provide the far-field gas phase temperature. In this step, the TGM [21] concept is adopted. TGM is an efficient coarse-graining method to deal with a large particle number, as the computational cost is independent from the particle number [13]. A particle grid is generated from the fluid grid. The particle grid cell size is larger than that of the fluid grid, and also larger than the particle diameter. There are no governing equations resolved on the particle grid. It is only used to transfer and average the gas information to the particles. Since the particle grid and the fluid grid are both fixed, one efficient way to map the gas data to the particle grid is to create a grid cell ID matching table before the simulation, as shown in Fig. 1. When the fluid grid cell is partially overlapped with different particle grid cells, it will be assigned to the closest particle grid cell according to its centroid. In such a situation, the particle grid cells represented by the ID matching table are approximations of the particle grid cells generated initially. This method is even more convenient when unstructured mesh is used for the fluid grid. After every fluid time step, the particle grid will collect the mean values according to the table.

The volumetric mean is used in the data mapping, and the gas phase properties can be calculated as:

$$\phi_{pg,i} = \frac{\sum_{\forall j \in pg,i} V_{fg,j} \phi_{fg,j}}{\sum_{\forall j \in pg,i} V_{fg,j}}, \tag{13}$$

where $\phi_{pg,i}$ and $\phi_{fg,j}$ represent any given gas phase property in ith particle cell and jth fluid cell, respectively, $V_{fg,j}$ is the cell volume of jth fluid cell. The gas phase properties includes temperature, species concentration, density and thermal-physical properties, such as heat capacity and heat conductivity.

The second part of the coupling is to transfer particle data to the CFD model. The data that needs to be transferred includes the mass and heat source terms (the momentum exchange between the gas and particle is neglected in this work), and the particle properties. These are, for example, the particle volume needed to obtain the phase fraction, the equivalent particle absorption coefficient and the equivalent particle scattering factor that are required by the gas phase radiation model, which will be presented in Section 2.3.1. Because the particle can be much larger than the fluid grid cell, the particle data need to be redistributed on the fluid grid. This redistribution should consider the particle's physical presence in space and the robustness of the solver, as well as introduce as little additional spatial diffusion of the data as possible. Consequently, the redistribution of the particle data needs to be confined to a relatively narrow region around the particle center. In this work, the diffusion-based method (DBM) proposed by Capecelatro et al. [22] and further developed by Sun et al. [12] is implemented. The particle data will be transferred to the fluid grid cell where its centroid is located, then, before the governing equations of the gas phase are solved, a diffusion operation is implemented by solving:

$$\frac{\partial S}{\partial \tau} = \nabla^2 S, \tag{14}$$

where τ is the diffusion time variable, and S represents any particle scalar data. The no-flux boundary condition should be applied to the computational domain to guarantee the conservation of the passive scalar S during such a diffusion operation. When the diffusion has been accomplished, the particle data will result in a distribution that is equivalent to the distribution with a Gaussian kernel [12,23]. For example, the scalar S can be the value of the particle's volume. After the diffusion operation, the redistributed S field divided by the volume field of the fluid grid cell represents the smoothed volume fraction field of the solid phase. The length scale b for this diffusion operation, which is equivalent to the bandwidth in Gaussian distribution, is determined by the total diffusion τ_{total} by $b = \sqrt{4\tau_{total}}$. For different particle data, a different length scale can be assigned by using different values of τ_{total}. The DBM smears particle data at each particle's position without calculation of massive grid searching, while the total particle number has little impact on the computational expenses [13]. The overall coupling method is illustrated in Fig. 2.

There are two main benefits of combining the TGM and the DBM. The first is that by choosing a proper τ_{total}, the DBM can avoid over-smearing the particle data instead of using the TGM also for the particle data redistribution. The second is that although a corresponding DBM sampling method for the gas phase properties is theoretically possible (e.g. to diffuse the gas data that are temporarily stored on a separate mesh at each time), many factors may influence the sampling results, such as mesh resolutions, mesh types, and diffusion operation parameters. Its numerical accuracy and efficiency have not been well studied. Previous works [23,24] using the DBM only applied the same sampling methods as the PCM. The TGM can sample the averaged gas phase properties with a much higher computational efficiency [13], which are less disturbed by the Gaussian distribution of the source terms.

It should be noted that the current approach lies between the traditional Eulerian-Lagrangian methods (e.g. particles are small in relation to the fluid cell sizes) and the particle-resolved methods (e.g. boundary-fitted grid or immersed-boundary methods and so on). This approach avoids the computationally heavy fully resolved calculation but is not able to fulfill the theoretical requirements of the Eulerian-Lagrangian approach. A certain degree of approximation has to be introduced, such as the particle grid size and the length scale b in the TGM and the DBM, respectively. The relation between the coupling parameters and their effects on the simula-

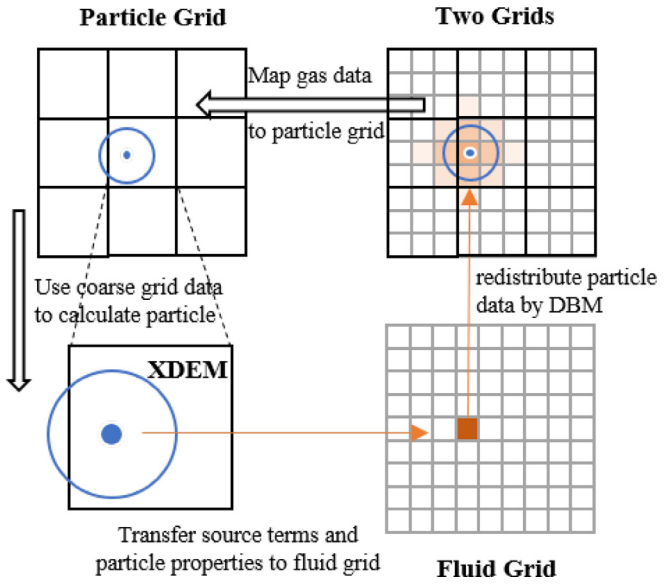

Fig. 2. Coupling method. The solid black lines are the particle grid, whereas the grey lines indicate the fluid grid.

tion needs to be analyzed. By identifying the intermediate coupling length as an independent parameter of the coupling model, the coupling effects and the grid independence for the CFD solver can be studied separately in different respects. As mentioned above, the relevant considerations when deriving the TGM and the DBM formulations are independent and possibly even partly contradictory. Thus, there is no reason to expect a priori that the same length scale should be used in these two aspects of the coupling.

2.3. Gas phase sub-models

2.3.1. Gas phase radiation model

The discrete ordinates (DO) model [25] is used to solve the radiative transfer equation (RTE) for the gas phase. Considering the particle effects, assuming the refractive index of the gas phase is 1, the RTE can be written as:

$$\nabla\cdot(I\vec{s})+(a_g+a_p+\sigma_p)I(\vec{r},\vec{s}) = a_g\frac{\sigma {T_g}^4}{\pi}+E_p + \frac{\sigma_p}{4\pi}\int_0^{4\pi} I(\vec{r},\vec{s}')\Phi(\vec{s}\cdot\vec{s}')d\Omega', \quad (15)$$

where I is the radiation intensity, a_g is the absorption coefficient of the gas phase, $\vec{s}$ and $\vec{r}$ are the direction and the position vectors, respectively, Φ is the scattering phase function, Ω is a solid angle, a_p, E_p and σ_p are the equivalent absorption coefficient, equivalent emission and equivalent particle scattering factor due to the presence of particles. Those equivalent coefficients will have influences on the transport of the radiation intensity, which can be regarded as the result of the blocking effect of particles on the gas phase radiative heat transfer. The finite-volume method (FVM) is used in OpenFOAM®to discretize Eq. (15), and the particles equivalent properties can be calculated by:

$$a_p=\sum_{i=1}^{N}\epsilon_{pi}\frac{A_{pi}}{V}, \quad (16)$$

$$A_{pi}=\frac{\pi d_{pi}^2}{4}, \quad (17)$$

$$E_p=\sum_{i=1}^{N}\epsilon_{pi}A_{pi}\frac{\sigma T_{pi}^4}{\pi V}, \quad (18)$$

$$\sigma_p=\sum_{i=1}^{N}\left(1-f_{pi}\right)\left(1-\epsilon_{pi}\right)\frac{A_{pi}}{V}, \quad (19)$$

where ϵ_{pi}, A_{pi}, T_{pi} and f_{pi} are the emissivity, projected area, surface temperature and scattering factor of particle i, V is the cell volume, and N is the number of the particles in the cell.

Since H_2O and CO_2 are the main products in the gas phase, the absorption coefficient has been assumed to be [26]:

$$a_g=0.1(w_{H_2O}+w_{CO_2}), \quad (20)$$

where w_{H_2O} and w_{CO_2} are the mass fraction of H_2O and CO_2, respectively.

2.3.2. Gas phase reactions

In our previous work [13], global reactions were used. However, in this study, the combustion is laminar and an accurate prediction of the ignition front is important. For this reason, a detailed reaction mechanism is used for the homogeneous reactions, namely the 32 species and 255 reactions set developed by Li et al. [27]. This detailed mechanism does however not include tar decomposition, and therefore reaction No.4 in Table 4 from [13] is added to the mechanism. To increase the simulation efficiency, the tabulation of dynamic adaptive chemistry (TDAC) method [28] is used.

2.4. Solution strategy

The particle collision sub-model requires particle searching, which is quite computationally costly. However, in a fixed-bed simulation, the particles are almost constantly in stagnant contacts. It is thus not necessary that the particle collision model is solved at every time step. Hence, only at a specified frequency is the particle motion sub-model that takes advantage of this pseudo-steady-state behavior applied. In every m fluid time steps, the particle motion sub-model is solved at the first n time steps (m and n are arbitrary integers, where $n < m$). For example, in this study, in every 100 fluid time steps, the particle motion can be resolved only at the first 20 time steps, then the computational expense of the particle motion sub-model is reduced to one-fifth. The fluid time steps for which the motion is not calculated, the contacts of the particle and the particle-particle contact radius $r_{c,ij}$ are kept the same as the last predictions from the particle motion sub-model, while other particle properties, such as, the particle temperature, will still be updated by solving the particle conversion sub-models. The values used in this study are based on our simulation experience. It is worth mentioning that such a calculation strategy is specifically designed for the solid phase with slow motion. If the particles movement is intense, for example, in a fluidized bed, this strategy should not be adopted. The XDEM could also use a smaller time step than the fluid time step. The overall calculation scheme is shown as follows.

1. Resolve the CFD model, update gas phase properties at the current fluid time.
2. Map the gas data to the particle grid and calculate the gas phase properties as seen by each particle.
3. Resolve particle conversion sub-models in one particle time step.
4. Resolve particle motion sub-model in one particle time step, if in this fluid time step it is required.
5. Advance to the next particle time step, and repeat steps 2 and 3, until the accumulated particle time steps equal the current fluid time step, then transfer particle data to the fluid grid.
6. Diffuse particle data from $t = 0$ s to τ_{total} s by DBM on the fluid grid.
7. Advance the CFD solver to the next fluid time.

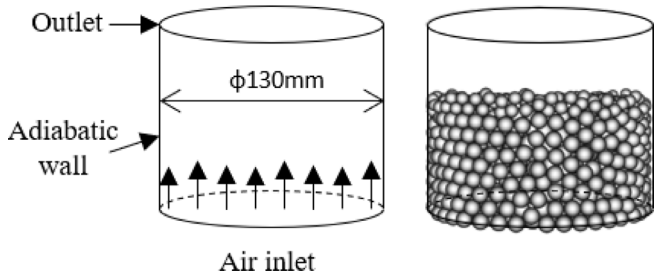

Fig. 3. Computational domain and boundary conditions.

Table 1
Particle physical properties.

	Value	Unit
Moisture	9.8	*w%*
Ash content	3.3	*w%*(dry basis)
Ash intrinsic density	2000	$kg \cdot m^{-3}$
Equivalent diameter, d_p	0.0084	m
Cylinder aspect ratio	1.67	-
Density of the particle	1030	$kg \cdot m^{-3}$
Shrinkage factor for char burnout	0.05-0.35	-
Ash layer porosity	calculated	-

3. Validation and sensitivity study

In order to validate the numerical model, important properties predicted by simulation are compared with the measurements of Porteiro et al. [29]. The experiment is set up as a fixed-bed combustion in a tube reactor. The ignition front propagates in the direction opposite to the airflow, which is known as counter-current mode. The front of conversion and ignition propagate downwards, which can be quantified by the measured ignited mass flux. The simulation domain is a section of the experimental setup. In accordance with the experiment, the geometry and boundary conditions are illustrated in Fig. 3.

Three different sets of fluid grids are generated for a grid independence test. The three grids have 79,920 (fine), 23,040 (medium) and 6,144 (coarse) cells, respectively. The corresponding mean cell side lengths are 2.6 mm, 3.9 mm and 6.1 mm, for the three grids. Additionally, a coarser grid (PCMGrid) is generated for the PCM simulation. Because PCM normally requires that the cell should be much larger than the particle size, the PCMGrid has 672 cells with a mean cell side length of 12.7 mm.

The thermophysical properties of the gas phase, as well as the calculation of reaction heat, are evaluated by the standard NASA polynomials [30]. The cases using poplar pellets as fuel [29] are chosen for validation. Some relevant particle properties are listed in Table 1. Other properties are the same as presented in our previous work (Table 5) [13].

In the simulation, 2000 poplar pellets were injected into the domain from the top, and the fuel bed was thus formed by means of a random stacking of particles through DEM calculation. In the experiments, the bed was ignited from the top. Correspondingly, the particles in the top layer of the fuel bed are initialized as char particles (particles that have accomplished drying and devolatilization) with a temperature of 1250 K, which is sufficient to start the char oxidation. For all the particle sub-models, a time step of 10^{-4} s is used, while for the CFD solver the time step is 10^{-3} s. The particle motion sub-model is solved in the first 20 time fluid steps for every 100 time steps.

For the DBM, the diffusion time τ_{total} was sub-divided into 6 shorter time steps. Different length scales (b) for the diffusion operation are adopted for different particle data. For the exchange source terms, $b = d_p$ is applied, because the interactions between the particle and the gas phase are expected to occur in the particle's local region, without being overlapped too much with its neighbors. While for the particle properties, like the particle volume, $b = 2d_p$ is applied, because the DBM is expected to smear the particle properties more smoothly in space to increase the robustness of the solver. TGM requires that the configuration of the size of the particle grid is defined in the coupling method. A sensitivity study was conducted, and the average side length of the particle grid cell of $1d_p$, $1.5d_p$ and $2d_p$ are compared. The default values for the particle grid size and for the shrinkage factor during char combustion are $1.5d_p$ and 0.3, respectively.

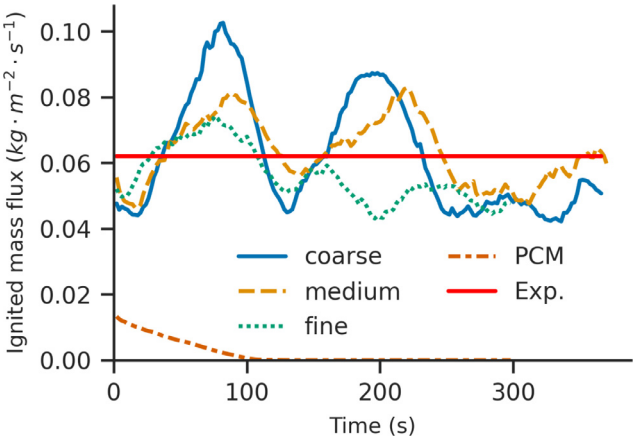

Fig. 4. Instantaneous ignited mass flux calculated using PCM and the proposed method with different grid resolution (data for Exp. is the mean ignited mass flux). The airflow rate is 0.276 $kg \cdot m^{-2} \cdot s^{-1}$, and the particle grid size is $1.5d_p$.

3.1. Grid sensitivity analysis

The combined TGM-DBM coupling method presented in Section 2.2 only works when the size of the particle grid is larger than the fluid grid. The three fluid grids with different resolutions are tested against the PCM on the PCM grid. The grid size for PCM is very close to the particle grid size. The transient ignited mass flux is shown in Fig. 4. The time-averaged ignited mass flux predicted by using fine, medium and coarse girds are 0.056, 0.063 and 0.064 $kg \cdot m^{-2} \cdot s^{-1}$, respectively, which are in good agreement with experimental observation. For the instantaneous ignited mass flux, the coarser grid predicted a larger oscillation.

As shown in Fig. 4, the PCM is found to fail in predicting the fixed-bed combustion. In the experiments, there will be an ignition front propagating downwards. Particles above the ignition front will release heat intensively due to the char burnout and the combustion of volatiles released in the devolatilization stage. In the PCM simulation, the computational cells are too large. The source terms in heat and species equations will be evenly redistributed into a correspondingly large space, resulting in an underestimation of the gas phase temperature. Then, the particle will be cooled down by convection, and the bed will be unable to sustain the propagation of the conversion front. It should be noted that if the TGM is used for both the sampling and redistribution, similar results will be obtained. Such deviations indicate the necessity of a proper coupling method in the simulation.

The predictions using the new coupling method with different fluid resolutions show a clear periodic trend in the ignited mass flux as shown in Fig. 4. The results have a similar period, which is related to the particle grid size as will be discussed in the later sections. Since the TGM coupling is implemented with the same coupling parameters for the different simulations, the differences are mainly due to that the DBM coupling has different perfor-

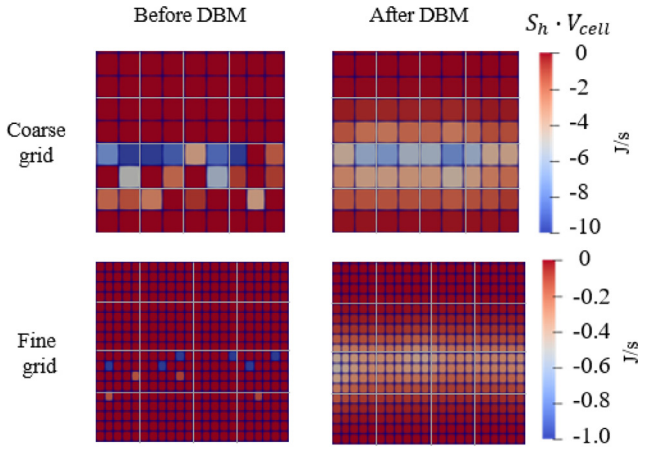

Fig. 5. Performance of DBM on different grids. The particle grid is marked in gray, and the fluid grid is marked in blue. (For interpretation of the references to colour in this figure legend, the reader is referred to the web version of this article.)

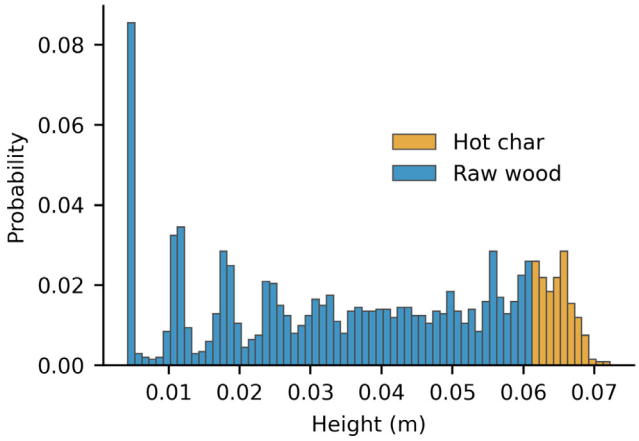

Fig. 6. The probability distribution of initial heights of particle centroids.

mances on the grids with different resolutions. Fig. 5 shows that the grid resolution has effects on the DBM coupling taking the energy source term (S_h) as an example. A particle whose centroid is located at the edge of a cell boundary of the particle grid, will have quite a different impact on the neighboring particle cells than if its centroid is placed closer to the center of the grid cell. With a finer fluid grid, the particle data are smeared more smoothly after the DBM has been applied, while with a coarser fluid grid, the particle's influence is still mainly on the particle grid, which holds the particle's centroid. In general, a finer fluid grid will reduce the gradient of gas phase properties on the particle grid. So, when the fluid grid becomes finer, the curves in Fig. 4 become more smooth. It is worth noting that a mesh-independent solution does not mean that the fluctuations are eliminated. The particle mass loss rate is very uneven, especially regarding different conversion sub-processes. So, such fluctuations could arise because of the discrete nature of the XDEM representation of the particles in the bed, and thus reflect a correct physical phenomenon. For example, when the width of the fixed-bed is quite limited, the packing of the particles with uniformed diameter will show the layering structure, as shown in Fig. 6. Then, the quasi-steady conversion will show a periodic character as the ignition front propagating layer by layer of the particles. In the simulation, the finer grid also requires a larger computational cost, especially for the DBM coupling. Considering all these effects, the medium fluid grid is chosen for the remainder of this study.

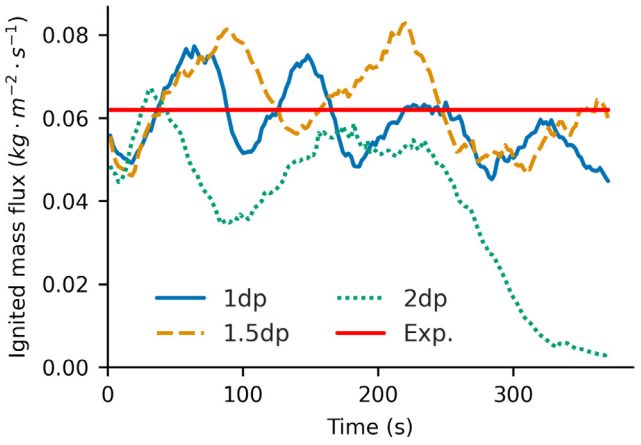

Fig. 7. Instantaneous ignited mass flux predicted by different sizes of particle grid (data for Exp. is the mean ignited mass flux). The airflow rate is 0.276 $kg \cdot m^{-2} \cdot s^{-1}$, and the fluid grid is medium.

3.2. Coupling parameters study

For the DBM coupling, the particle is already much larger than the fluid grid cell and the major concern is therefore that the smoothing of the source terms should not cause excessive numerical diffusion. Large positive source terms will exacerbate solver robustness [31], thus there are usually strong arguments for extensive smoothing from a stability perspective. As discussed above, due to that the particles are in direct contact with each other, the particle's direct influence will be limited to the region close to its surface. There is not much free void space to motivate changing to a different length scale for the source terms other than $b = d_p$. As long as the particle properties are changing smoothly in relation to the gas phase, it will also enhance the robustness of the solver.

The primary use of the particle grid is used to calculate the means of the gas data as seen by the particles. In the fixed-bed simulation, if the particle grid cell is larger than 2 times the particle diameter, the influence from the neighboring particles will be larger than what is typically possible to motivate from physical arguments for the targeted particle. The gas phase beyond the particle's first neighbors is unlikely to have direct interaction with the particle.

The predicted transient ignited mass fluxes with different particle grid sizes are shown in Fig. 7. In the first 300 s, the result using $1d_p$ particle grid size has 3 periods, while the result using $1.5d_p$ particle grid has 2 periods. The periods are exactly inversely proportional to the particle grid size, showing that the choice of particle grid spacing will significantly influence the states of transient simulation. However, the time-averaged ignited mass flux from the two predictions are quite close (0.63 and 0.60 $kg \cdot m^{-2} \cdot s^{-1}$, for $1.5d_p$ and $1d_p$ case, respectively), while for the prediction with $2d_p$ particle grid, it seems that the convective cooling is overestimated in the same way as in the PCM predictions. In this study, the particle grid size of $1.5d_p$ was selected for further investigation, as its prediction agrees with the experimental measurement. At the same time, the chosen grid size is more in correspondence with the model assumption that the particle grid size should be larger than the particle size.

3.3. Sensitivity study on particle shrinkage factor

Unlike the particle shrinkage during the drying and devolatilization process, the changing volume related to char conversion is associated with a larger uncertainty. It is not only related to the ash content but is also affected by the combustion temperature

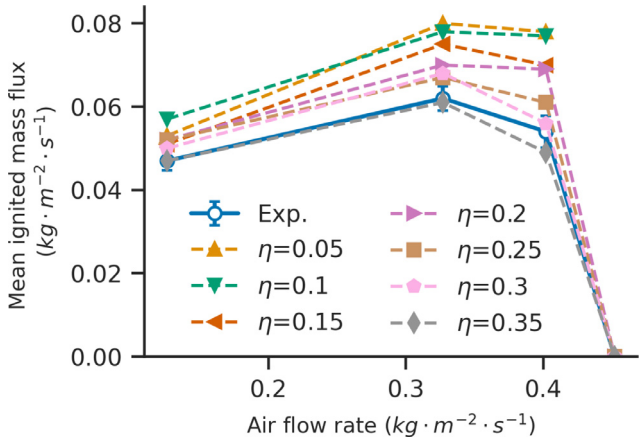

Fig. 8. Mean ignited mass flux predicted with different shrinkage factors for the char conversion process. The particle grid size is $1.5d_p$ and the fluid grid is medium.

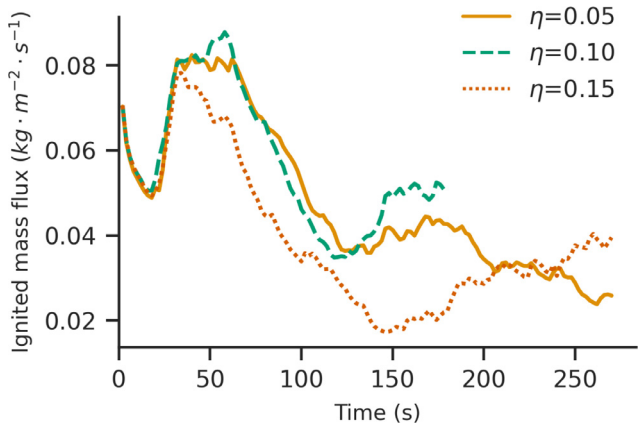

Fig. 9. The influence of shrinkage factors (η = 0.05, 0.1, and 0.15) on instantaneous ignited mas flux at an airflow rate of 0.452 $kg \cdot m^{-2} \cdot s^{-1}$.

and even the encapsulation of the material [32]. The shrinkage factor for the char conversion process (η) will eventually determine the volume of the ash layer and the particle's outermost surface area, which is critical in the calculation of the heat transfer with the gas phase and neighboring particles. A series of shrinkage factors for the char conversion process are tested under four operating conditions, which are oxygen limited, reaction limited, cooling by convection and blown-off conversion regimes.

The predictions of the mean ignited mass fluxes together with the experimental measurements are shown in Fig. 8. The overall trend is that the bed conversion rate increases with the decrease of η. Because η only affects the volume of the ash layer, it will have no influence on the char layer surface area. By definition, a smaller η means a smaller eventual particle volume. During char burnout, a smaller outermost surface area will reduce the cooling through convective heat transfer with the gas phase. Then, the particle's surface temperature will be overestimated. In Fig. 8, for η equal to 0.05, 0.1 and 0.15, the predictions at the highest airflow rates are absent, because in these three cases the simulations are quite unstable, which means that the periodical changing of the ignited mass flux is not established, as shown in Fig. 9.

For η = 0.15, the bed temperatures at 50 s, 150 s and 250 s are shown in Fig. 10. The bed is not totally extinguished at the high airflow rate. Along the wall region where the gas velocity is rather low, the bed conversion is still self-sustained. A small η also helps the char particle, which is at the last conversion stage with a small volume, fill into the gaps in the next particle layer. More detailed

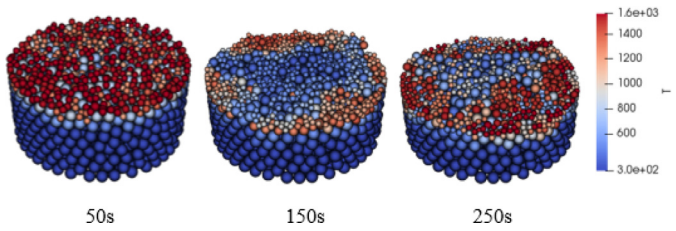

Fig. 10. Particle temperature at 50, 150, and 250 s after the ignition of the bed (η = 0.15).

experimental observation is needed to validate this phenomenon. Johansson et al. [33] also pointed out that the ash properties are critical in determining the burning velocity and extinction phenomena at high airflow rates, by affecting the radiative heat transfer in the bed in their simulation of fixed-bed combustion through a PMM approach. The sensitivity analysis on η indicates that the model of the morphology of the ash layer could play an important role in such XDEM/CFD modeling on the fixed-bed combustion. A shrinkage factor between 0.25 and 0.35 results in a good agreement with the experimental measurements. In this study, η = 0.3 is adopted in the later simulations, and the final volume changing is in a reasonable range considering the ash content [34].

4. Results and discussion

4.1. Ignited mass flux

From the above sections, the following simulations were configured with the medium fluid mesh, $1.5dp$ particle grid, and η=0.3. The predicted mean ignited mass fluxes at all measured airflow rates are shown in Fig. 11. The excess air ratios are calculated with regard to the stoichiometric air (5.59 *kg* of dry air per *kg* of fuel burnt) which is determined by the chemical equivalent formula of the poplar pellets ($CH_{1.55}O_{0.75}$, major elements only) [29]. The predictions by the developed XDEM/CFD model are in very good agreement with the experimental measurements. The slopes in the three combustion zones, which include oxygen limited, reaction limited and cooling by convection, are well captured, as well as the extinction at a high airflow rate.

In the reaction limited zone, simulations predict a small increase in the mean ignited mass flux, which is significantly lower than in the oxygen-limited regime, but somewhat higher than that observed in the experiments. We looked further into these deviations and observed that they originate from the TGM coupling and the particle surface mass transfer sub-model. Firstly, the mean O_2 concentration calculated on the particle grid, which is needed for the particle conversion sub-model, is not equal to that infinitely far away from the particle surface, as is assumed in the theoretical underlying derivation of the sub-model [13]. This fact implies that the far-field concentration employed in the sub-model will be lower than that at the inlet, and will increase with the inlet flow rate. Secondly, compared to the mass diffusion through the ash layer, the mass diffusion from the gas phase to the particle surface is the dominating process. The mass transfer coefficient h_m calculated from Eq. (12) is increasing as the gas velocity increases. The char conversion rate is directly determined by the above two variables [4]. Still, it is concluded that the deviations in the reaction limited zone are acceptable.

4.2. The coupling effects

The instantaneous ignited mass flux by process contribution predicted in the case where the airflow rate is 0.327 $kg \cdot m^{-2} \cdot s^{-1}$ (referred to as the reaction limited case later) is shown in Fig. 12.

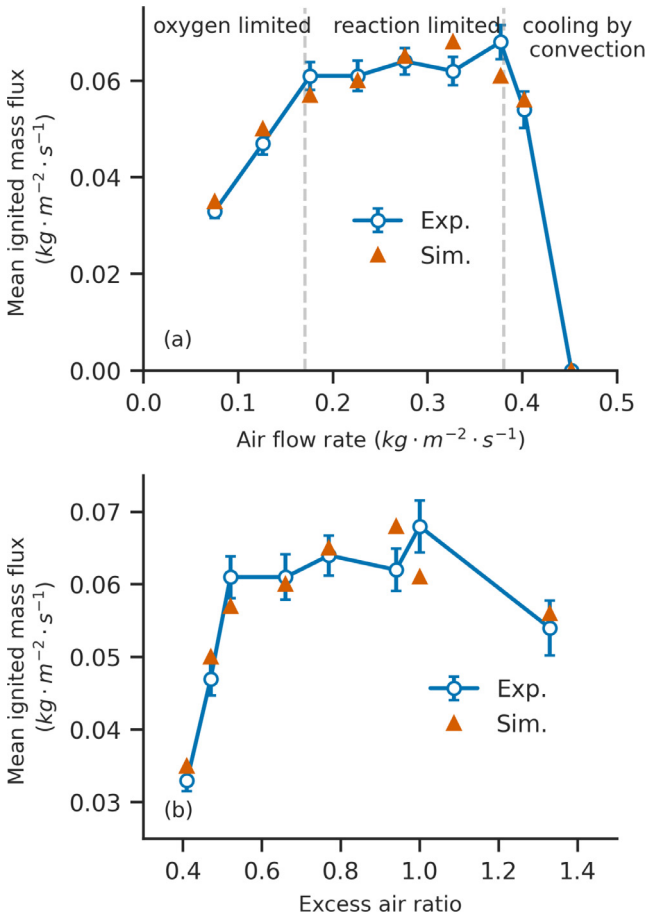

Fig. 11. Mean ignited mass flux at different airflow rates (a) and excess air ratios (b).

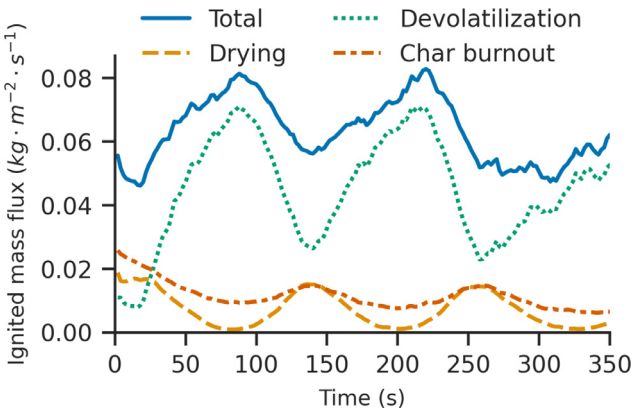

Fig. 12. Instantaneous ignited mass flux including the contribution from each subprocess at an airflow rate of 0.327 $kg \cdot m^{-2} \cdot s^{-1}$ (reaction limited case).

The majority of the mass loss is through the devolatilization process. In each given period, the conversion rates of the drying and char burnout processes change oppositely to the rate of the devolatilization process. Such periodic oscillation is strongly related to the particle grid configuration. From the bottom of the bed to the height of 0.06 m, there are 5 layers of particle grid cells in the vertical direction. The thermal conversion process in these grid layers is illustrated in Fig. 13 in terms of particle temperature and conversion ratio, respectively.

The colored regions in Fig. 13 mark the boundaries of the particle's status distribution at certain points in time. The layers are referred to as 1st to 5th layer particle cells for convenience. At 50 s, the conversion rate of devolatilization is increasing, while the drying and char burnout rates are decreasing. Fig. 13 shows that at 50 s, in the 4th particle cells at the height around 0.04-0.05 m, the temperature difference between the particles can indeed be quite large. Except for the char particles, most particles in these particle cells just completed drying or are still in the drying process. At this stage, the particles contain mainly the dry wood. There is a clear drying front at the height of around 0.04 m that temporarily stopped between the 3rd and 4th layer of the particle cells. At 100 s, the particles in the 3rd layer of the particle cells started the drying process. The dry wood in the 4th layer of the particle cells is still being consumed. When the devolatilization rate decreases, more O_2 could join the char burnout instead of the homogeneous gas phase reactions with the released pyrolysis gases. At 200 s, Fig. 13 shows a clear stagnation of the propagation of the drying front again.

The size of the particle grid cells is designed to be larger than the length scale of the conversion front, and as a result the front will either be smoothed out or move discretely at a length scale dictated by the mesh size. The gas phase temperature is critical in the prediction of the drying process, and the numerical effects introduced by the coupling scheme consequently produce feedback effects in the modeling prediction of the bed conversion processes. As a summary, the coupling effect of the TGM shows that an accurate, mesh-independent prediction of the location of the drying front is hard to achieve.

4.3. Heat contribution in fixed-bed combustion of biomass

The particles whose initial centroid positions are located between 0.039 m and 0.042 m (in the 4th layer of the particle cells, 340 particles) are tracked for their entire conversion process in an effort to quantify particle-level variations, something that the XDEM/CFD approach intrinsically incorporates but which is filtered out in Eulerian methods. For every particle, the particle conversion time count starts only at the onset of thermal conversion (when conversion equals 0.005). For the reaction limited case, the particle conversion ratio and surface temperature versus the conversion time are shown in Figs. 14 and 15. The shadowed region shows the boundaries of the distribution, and the evolution of three representative particles is also plotted as solid lines in the figures.

Particles A, B and C are identified to show different conversion histories. They can be described as a fast converting particle, medium converting particle and slow converting particle, respectively. The main difference is observed in the drying process because for the devolatilization and char burnout processes, the curves in Fig. 14 show similar slopes. Fig. 15 reveals that in the drying process different particles experience rather different heating rates. After the devolatilization, when the char burnout starts, there is a sudden temperature jump. The temperatures remain similar during the char burnout phase for the different particles.

The heat contribution terms in Eq. (3), together with the combustion heat, which is released from the char burnout process, for particles A, B and C are shown in Figs. 16, 17 and 18, respectively. The fast converting particle is directly contacted to the high temperature char particles. The particle is heated up mainly through particle to particle radiation, while due to the fresh airflow from the bottom, the convection by the gas acts as cooling the particle. For the medium converting particle, it is not directly in contact with any char burning particles, but it belongs to a particle cell that includes high-temperature regions. Convection and radiation have similar contributions to the particle temperature rise. It is shown in Fig. 17, particle B experienced a reignition at around 160 s. This is because, at this moment, particle B moved from a particle grid cell in the 4th particle cell layer to another one in

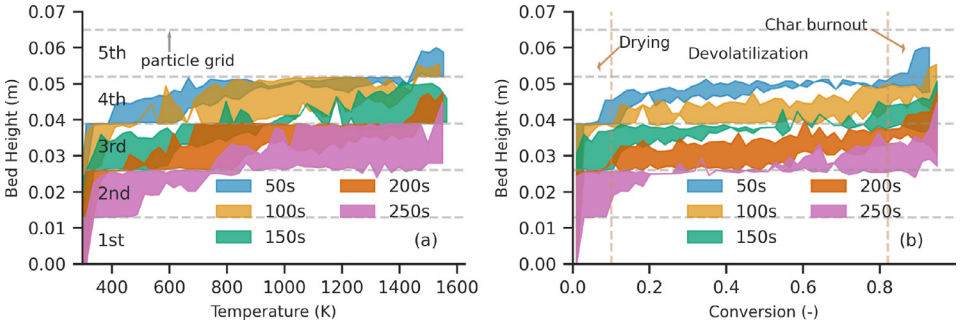

Fig. 13. Particle temperature (a) and conversion (b) along with the bed height at selected points in time for the reaction limited case. Two vertical dashed lines approximately separate the conversion into three stages: drying, devolatilization, and char burnout. The left vertical dashed line is based on the moisture content, and the right vertical dashed line is based on the average char yield.

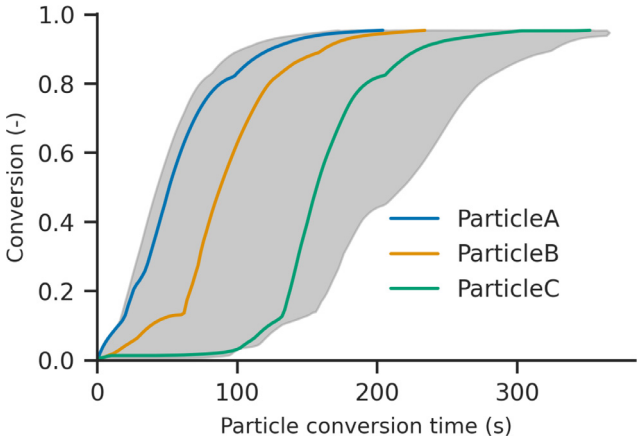

Fig. 14. Particle conversion versus conversion time for the reaction limited case.

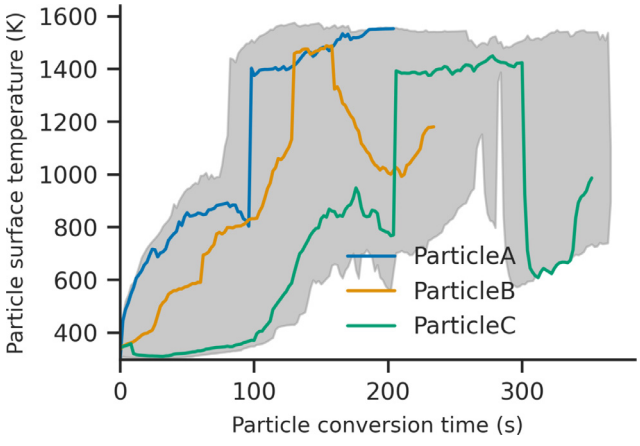

Fig. 15. Particle surface temperature versus conversion time for the reaction limited case.

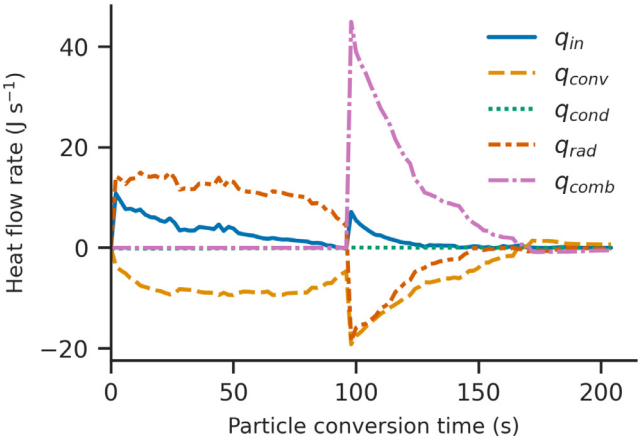

Fig. 16. Heat flow rate of different mechanisms for particle A.

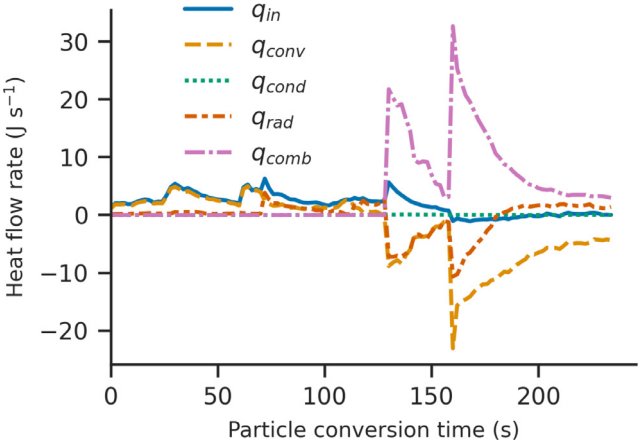

Fig. 17. Heat flow rate of different mechanisms for particle B.

the 3rd layer which has a higher O_2 concentration. For the slow converting particle, it is very likely that at the beginning of the period, it is in contact with particles that are going through the devolatilization process. The temperature of the particle undergoing devolatilization is mainly in the range of 600-800K. The heating process is rather slow. However, when its neighbors complete devolatilization, and start char burnout, the slow converting particle will start to behave like the fast converting particle. In the char burnout stage, both convection and radiation contribute to the cooling of the particle. As shown in Figs. 16, 17 and 18, the heat transfer due to the particle to particle conduction can be neglected for all three particles. Other studies also indicate similar findings, as for example by Shin et al. [34]. However, it is still possible that in the present study the particle to particle heat conduction is underestimated by current sub-models.

The case with the airflow rate of 0.126 $kg \cdot m^{-2} \cdot s^{-1}$ is referred to as representative of the oxygen limited case. A comparison between the oxygen limited case and the reaction limited case on the particle conversion process is shown on Fig. 19. A large part of the particle conversion processes are overlapping, however, during the char burnout stage, the oxygen limited case has a lower ignited mass flux, and the particles conversion rates are much lower.

The probability distributions of the heat contribution for the tracked particle are shown in Figs. 20–23. Figs. 20 and 22 show

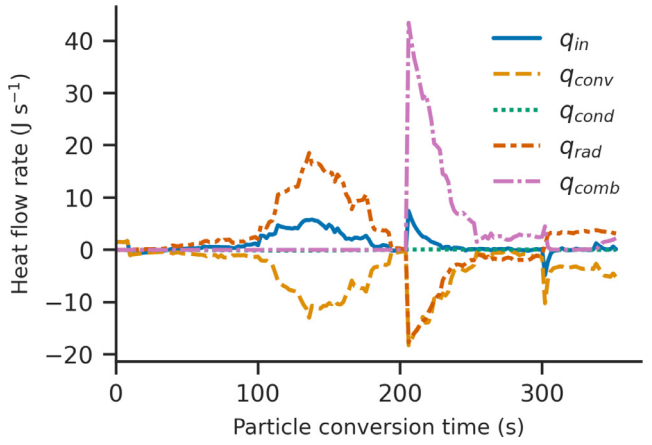

Fig. 18. Heat flow rate of different mechanisms for particle C.

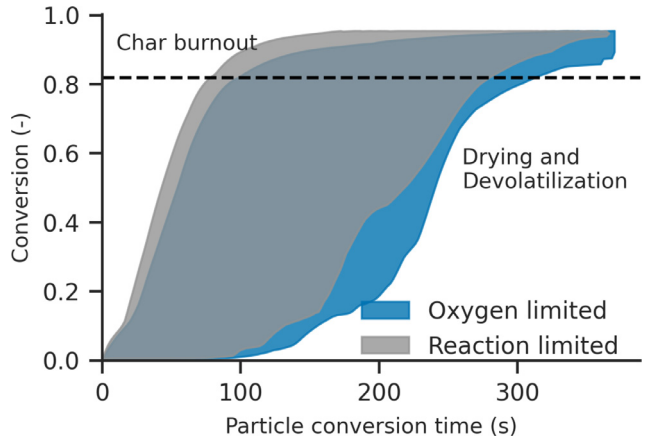

Fig. 19. Particle conversion versus conversion time for the reaction limited case and the oxygen limited case.

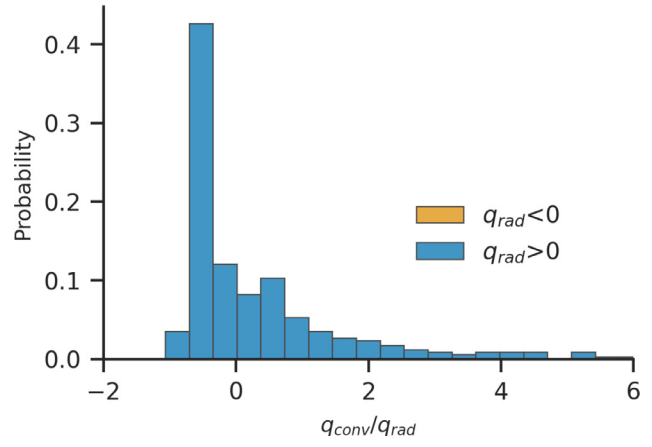

Fig. 20. Contribution from different heat exchange mechanisms during drying and devolatilization for the reaction limited case.

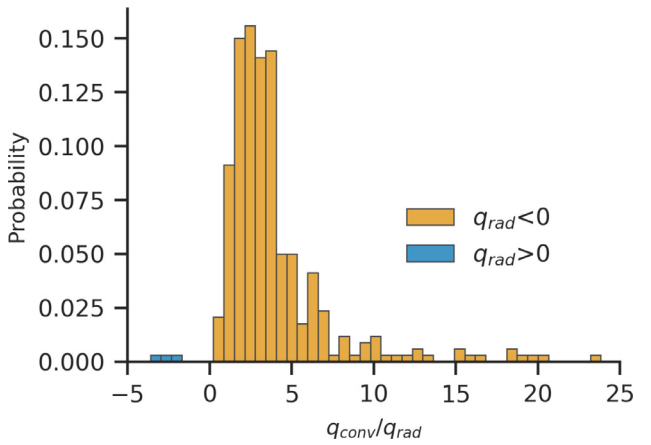

Fig. 21. Contribution from different heat exchange mechanisms during combustion for the reaction limited case.

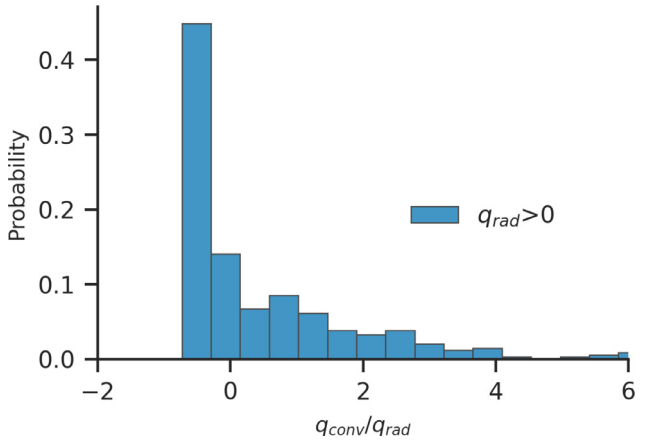

Fig. 22. Contribution from different heat exchange mechanisms during drying and devolatilization for the oxygen limited case.

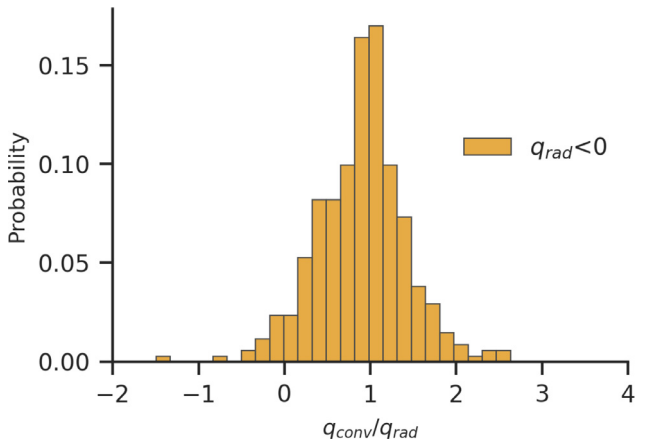

Fig. 23. Contribution from different heat exchange mechanisms during combustion for the oxygen limited case.

the ratio between convection and radiation heat flow rates during the drying and devolatilization processes for the reaction limited case and the oxygen limited case, respectively. In both cases, radiation is the main contributor to heat source terms. Nearly half of the particles lost heat through convection (where q_{conv}/q_{rad} is negative while q_{rad} is positive). Compared with the reaction limited case, the convective heating contributes more to the particle temperature increase in the oxygen limited cases. For the char burnout stage, the heat transfer from the particle to the environment is mainly archived by convection and radiation. For the reaction limited case, the convective cooling is much stronger than the radiative cooling, which is quite as expected.

5. Conclusion

An XDEM/CFD model for the simulation of biomass combustion in a fixed-bed has been developed, with a specific emphasis

on the coupling between the gas phase and the fuel particles. A combined coupling strategy of TGM and DBM is implemented to strike an optimal balance between computational efficiency, solver robustness and prediction accuracy. The inter-particle heat conduction and radiation are considered and coupled to the calculation of the DEM. Furthermore, the sensitivity of the obtained results to the coupling parameters is studied. The developed model enables the use of fluid grid resolution that is significantly smaller than the particle diameter.

To validate the proposed XDEM/CFD model, a laboratory-scaled fixed-bed experiment using poplar pellets as fuel is simulated. The side length of the particle grid cell is recommended to be 1.5 times the particle diameter since a much coarser grid leads to failure to predict the propagation of the ignition front. The shrinkage factor for the char burnout process has a notable influence on the simulation, where a smaller shrinkage factor tends to cause an overestimation of the bed ignition rate.

The model is able to capture the different conversion regimes under different operating conditions, which include oxygen limited conversion, reaction limited conversion, cooling by convection and extinction. The predicted time-averaged results are in good agreement with the experimental measurements, while the transient fluctuations observed in the bed are still influenced by the simulation settings of the TGM coupling. Therefore, the TGM coupling must be carefully treated. During the bed combustion, the conductive heat transfer between the particles can be neglected. More particles are heated up through the radiative heat transfer rather than the convective heat transfer. In the reaction limited conversion, the convective cooling is much stronger than the radiative cooling for most particles. However, the model has difficulties in capturing the exact spatial location of the drying front, a limitation induced by the TGM model itself. A gas to particle coupling model that can capture a smaller temperature gradient in the gas phase is needed to solve this issue.

Declaration of Competing Interest

The authors declare that they have no known competing financial interests or personal relationships that could have appeared to influence the work reported in this paper.

Acknowledgments

The authors acknowledge the financial support by the Knowledge-Building Project GrateCFD (267957), which is funded by LOGE AB, Statkraft Varme AS, EGE Oslo, Vattenfall AB, Hitachi Zosen Inova AG and Returkraft AS together with the Research Council of Norway through the ENERGIX program. UNINET Sigma2 and NTNU HPC Group provided high-performance computational resources for CFD simulations. Henrik Ström gratefully acknowledges co-financing from the Centre for Combustion Science and Technology (CECOST) and the Swedish Gasification Centre (SFC).

Appendix A. Particle sub-models

A conceptual illustration of the layout of the cylinder-shaped particle model is provided in Fig. A1. It is a 1-dimensional model in the radial direction. The intra-particle heat transfer is considered. The heat conservation equation is given by:

$$\frac{\partial \rho C_p T}{\partial t} = -\nabla \cdot q + S + \Delta Q, \tag{21}$$

where ρ is the particle density, C_p is the particle heat capacity, q is the conductive heat transfer, S is the heat source or sink term, and ΔQ is the reaction heat on the boundaries. The particle consists of four layers, and it is assumed that each layer has uniform properties. Eq. (21) is discretized based on the locations of the conversion front and the midpoint of each layer. No heat is accumulated at the conversion fronts. Thus, for the fronts, the left-hand side of Eq. (21) is 0, while for the layers, the reaction heat ΔQ is 0.

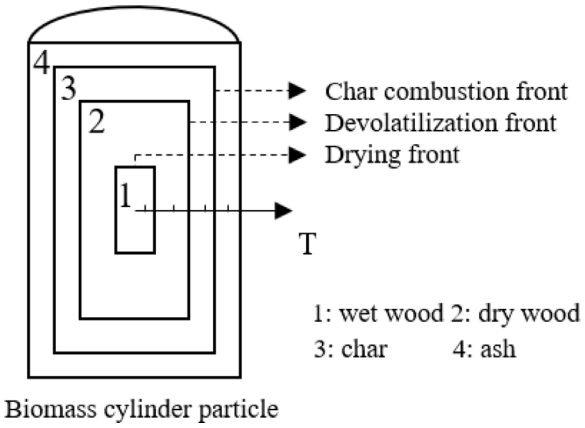

Fig. A1. Particle model layout.

The mass balance for each layer is based on the calculated reaction rate of each conversion front. However, the volume of each layer is calculated independently, which results in changing the density of each layer. Similar to Thunmans method [35], a shrinkage model using empirical shrinkage factors, η_i, is employed to update the particle volume according to the mass changes. The volume change of the ith layer, ΔV_{pi} is calculated by:

$$\Delta V_{pi} = \frac{\Delta m_{pi-1}}{\rho_{i-1}} \eta_i - \frac{\Delta m_{pi}}{\rho_i} \tag{22}$$

where Δm_{pi} is the mass consumed on the ith boundary. Every time step, after calculating the mass and volume of each layer, the density of each layer also needs to be updated.

A thermal drying model [36] is employed for the drying process. For the devolatilization process, a two-stage wood devolatilization model is adopted [37]. In the first stage, dry wood is decomposed into light gases, tar, and char through three competing parallel reactions. In the second stage, a part of the tar is further converted into light gases and char. Both of these two stages are considered to occur inside the particle. Tar released from the particle is treated as a gas product. Char burnout is considered as a surface reaction. Thunmans model for char conversion [35] is employed in this study. The char reaction process is a diffusion-controlled process. Since the ash layer is also considered in this study, the diffusion rate has contributions from both the diffusion of gases to the particle surface and the diffusion through the ash layer. The effective diffusivity of the species in the ash layer, $D_{e,ash}$, can be calculated by [38]:

$$D_{e,ash} = \varepsilon_{ash}^2 D_a, \tag{23}$$

where ε_{ash} is the porosity of the ash layer, and D_a is the molecular diffusivity of the penetrating gaseous component.

References

[1] M.R. Karim, J. Naser, CFD modelling of combustion and associated emission of wet woody biomass in a 4 MW moving grate boiler, Fuel 222 (2018) 656–674.
[2] H. Sefidari, N. Razmjoo, M. Strand, An experimental study of combustion and emissions of two types of woody biomass in a 12-MW reciprocating-grate boiler, Fuel 135 (2014) 120–129.
[3] H. Ström, H. Thunman, Cfd simulations of biofuel bed conversion: a submodel for the drying and devolatilization of thermally thick wood particles, Combust. Flame 160 (2) (2013) 417–431.
[4] S. Hermansson, H. Thunman, Cfd modelling of bed shrinkage and channelling in fixed-bed combustion, Combust. Flame 158 (5) (2011) 988–999.

[5] N.T.M. Duffy, J.A. Eaton, Investigation of factors affecting channelling in fixed-bed solid fuel combustion using CFD, Combust. Flame 160 (10) (2013) 2204–2220.
[6] B. Peters, Measurements and application of a discrete particle model (DPM) to simulate combustion of a packed bed of individual fuel particles, Combust. Flame 131 (1–2) (2002) 132–146.
[7] C. Bruch, B. Peters, T. Nussbaumer, Modelling wood combustion under fixed bed conditions, Fuel 82 (6) (2003) 729–738.
[8] J. Wiese, F. Wissing, D. Höhner, S. Wirtz, V. Scherer, U. Ley, H.M. Behr, Dem/cfd modeling of the fuel conversion in a pellet stove, Fuel Process. Technol. 152 (2016) 223–239.
[9] A.H. Mahmoudi, F. Hoffmann, M. Markovic, B. Peters, G. Brem, Numerical modeling of self-heating and self-ignition in a packed-bed of biomass using XDEM, Combust. Flame 163 (2016) 358–369.
[10] F. Wissing, S. Wirtz, V. Scherer, Simulating municipal solid waste incineration with a DEM/CFD method–influences of waste properties, grate and furnace design, Fuel 206 (2017) 638–656.
[11] R. Mehrabian, A. Shiehnejadhesar, R. Scharler, I. Obernberger, Multi-physics modelling of packed bed biomass combustion, Fuel 122 (2014) 164–178.
[12] R. Sun, H. Xiao, Diffusion-based coarse graining in hybrid continuum–discrete solvers: theoretical formulation and a priori tests, Int. J. Multiphase Flow 77 (2015) 142–157.
[13] J. Zhang, T. Li, H. Ström, T. Løvås, Grid-independent eulerian-lagrangian approaches for simulations of solid fuel particle combustion, Chem. Eng. J. 387 (2020) 123964.
[14] S. Ergun, Fluid flow through packed columns, Chem. Eng. Prog. 48 (1952) 89–94.
[15] C.Y. Wen, Mechanics of fluidization, Chem. Eng. Prog. Symp. Ser., volume 62 (1966), pp. 100–111.
[16] C. Fernandes, D. Semyonov, L.L. Ferrás, J.M. Nóbrega, Validation of the CFD-DPM solver DPMFoam in openFOAM®through analytical, numerical and experimental comparisons, Granular Matter 20 (4) (2018) 64.
[17] T. Li, H. Thunman, H. Ström, A fast-solving particle model for thermochemical conversion of biomass, Combust. Flame 213 (2020) 117–131.
[18] A. Singhal, S. Cloete, S. Radl, R. Quinta-Ferreira, S. Amini, Heat transfer to a gas from densely packed beds of cylindrical particles, Chem. Eng. Sci. 172 (2017) 1–12.
[19] G.K. Batchelor, R.W. O'brien, Thermal or electrical conduction through a granular material, Proc. R. Soc. Lond. A Math. Phys. Sciences 355 (1682) (1977) 313–333.
[20] Z. Zhou, A.B. Yu, P. Zulli, Particle scale study of heat transfer in packed and bubbling fluidized beds, AlChE J. 55 (4) (2009) 868–884.
[21] S. Deb, D.K. Tafti, A novel two-grid formulation for fluid–particle systems using the discrete element method, Powder Technol. 246 (2013) 601–616.
[22] J. Capecelatro, O. Desjardins, An euler–lagrange strategy for simulating particle-laden flows, J. Comput. Phys. 238 (2013) 1–31.
[23] H. Wu, N. Gui, X. Yang, J. Tu, S. Jiang, A smoothed void fraction method for CFD-DEM simulation of packed pebble beds with particle thermal radiation, Int. J. Heat Mass. Transf. 118 (2018) 275–288.
[24] R. Sun, H. Xiao, Diffusion-based coarse graining in hybrid continuum–discrete solvers: applications in CFD–DEM, Int. J. Multiphase Flow 72 (2015) 233–247.
[25] W.A. Fiveland, Discrete-ordinates solutions of the radiative transport equation for rectangular enclosures (1984).
[26] B.F. Magnussen, B.H. Hjertager, On mathematical modeling of turbulent combustion with special emphasis on soot formation and combustion, Symposium (international) on Combustion, volume 16, Elsevier (1977), pp. 719–729.
[27] T. Li, O. Skreiberg, T. Løvås, P. Glarborg, Skeletal mechanisms for prediction of NOx emission in solid fuel combustion, Fuel 254 (2019) 115569.
[28] Z. Li, M.T. Lewandowski, F. Contino, A. Parente, Assessment of on-the-fly chemistry reduction and tabulation approaches for the simulation of moderate or intense low-oxygen dilution combustion, Energy Fuels 32 (10) (2018) 10121–10131.
[29] J. Porteiro, D. Patino, J. Collazo, E. Granada, J. Moran, J.L. Miguez, Experimental analysis of the ignition front propagation of several biomass fuels in a fixed-bed combustor, Fuel 89 (1) (2010) 26–35.
[30] J. McBride, A. Reno, Coefficients thermodynamic properties for calculating and transport of individual species, Nasa Tech. Memo 4513 (1993) 98.
[31] C. Lian, G. Xia, C.L. Merkle, Impact of source terms on reliability of CFD algorithms, Comput. Fluids 39 (10) (2010) 1909–1922.
[32] R. Chirone, P. Salatino, F. Scala, R. Solimene, M. Urciuolo, Fluidized bed combustion of pelletized biomass and waste-derived fuels, Combust. Flame 155 (1–2) (2008) 21–36.
[33] R. Johansson, H. Thunman, B. Leckner, Influence of intraparticle gradients in modeling of fixed bed combustion, Combust. Flame 149 (1–2) (2007) 49–62.
[34] D. Shin, S. Choi, The combustion of simulated waste particles in a fixed bed, Combust. Flame 121 (1–2) (2000) 167–180.
[35] H. Thunman, B. Leckner, F. Niklasson, F. Johnsson, Combustion of wood particles-a particle model for eulerian calculations, Combust. Flame 129 (1–2) (2002) 30–46.
[36] H. Ström, H. Thunman, A computationally efficient particle submodel for CFD-simulations of fixed-bed conversion, Appl. Energy 112 (2013) 808–817.
[37] H. Lu, W. Robert, G. Peirce, B. Ripa, L.L. Baxter, Comprehensive study of biomass particle combustion, Energy Fuels 22 (4) (2008) 2826–2839.
[38] G.F. Froment, K.B. Bischoff, J. De Wilde, Chemical Reactor Analysis and Design, volume 2, Wiley New York, 1990.